

1 INTRODUCTION

2 Above Earth's atmosphere are the Van Allen radiation belts, a toroidally-shaped
3 pair of belts that consist of a complex and dynamic plasma environment. The inner
4 radiation belt consists of mostly energetic protons, is very stable on year time scales,
5 and is located within 2 Earth radii (measured near the equator) above Earth's Earth's
6 surface. The outer radiation belt, on the other hand, consists of mostly energetic
7 electrons, is highly dynamic on day, and even hour time scales, and is typically
8 found between 4 and 8 Earth radii above Earth's surface. The radiation belts pose a
9 challenge to space exploration due to their effects on our technology-driven society.
10 Some of the effects include: a higher radiation dose for astronauts and cosmonauts,
11 degradation of silicon to the point where transistors malfunction, computer memory
12 corrupts due to bit flips, etc. With these effects in mind, it is no surprise that the
13 radiation belts have been extensively studied since their discovery in the 1960s.

14 The radiation belt plasma is at times unstable which in turn generate electric and
15 magnetic waves. These waves in turn accelerate and scatter radiation belt particles
16 with a variety of wave-particle mechanisms. One form of wave-particle interactions
17 scatter particles into Earth's atmosphere in the form of electron microbursts.

18 Electron microbursts, henceforth referred to as microbursts, are typically
19 observed by low Earth orbiting spacecraft, sounding rockets, and high altitude
20 balloons as a sub-second impulse of electrons. Some of the most intense microbursts
21 have electron fluxes that are a factor of 10 to 100 above the background (for example
22 see Fig. 7 in Blake et al. (1996)). Since they were first reported by Anderson and
23 Milton (1964), the intense transient nature of microbursts have compelled countless
24 researchers to understand their properties, their effects on the environment, and the
25 physical mechanism(s) that create microbursts. Microbursts are widely believed

26 to be created by wave-particle scattering between a plasma wave called whistler
 27 mode chorus and outer radiation belt electrons, although many details regarding the
 28 scattering mechanism are unconstrained or unknown. The goal of this dissertation is
 29 to study the wave-particle scattering mechanism that scatters electron microbursts.

30 This chapter serves as an introduction to the fundamental physical concepts
 31 that are essential to understand wave-particle interactions in Earth's magnetosphere.
 32 We will first derive the motion of individual charged particles in Earth's electric and
 33 magnetic fields. Next we will cover how various groups of charged particles coalesce
 34 to form the major particle populations in the magnetosphere. Then, we will cover
 35 the various mechanisms that accelerate and scatter particles in the magnetosphere.
 36 Lastly, we will review microbursts, which is one of the loss mechanism, as a jumping-
 37 off point for the rest of the dissertation.

38 Charged Particle Motion in Electric and Magnetic Fields

A charged particle trapped in the magnetosphere will experience three types of periodic motion in Earth's nearly dipolar magnetic field. The three motions are ultimately due to the Lorentz force that a particle of momentum \vec{p} , charge q , and velocity \vec{v} experiences in an electric field \vec{E} and magnetic field \vec{B} and is given by

$$\frac{d\vec{p}}{dt} = q(\vec{E} + \vec{v} \times \vec{B}). \quad (1.1)$$

39 In the magnetosphere, the three periodic motions, in decreasing frequency, are
 40 gyration, bounce, and drift and are schematically shown in Fig. 1.1. Each periodic
 41 motion has a corresponding conserved quantity i.e. an adiabatic invariant.

The highest frequency periodic motion is gyration about a magnetic field of

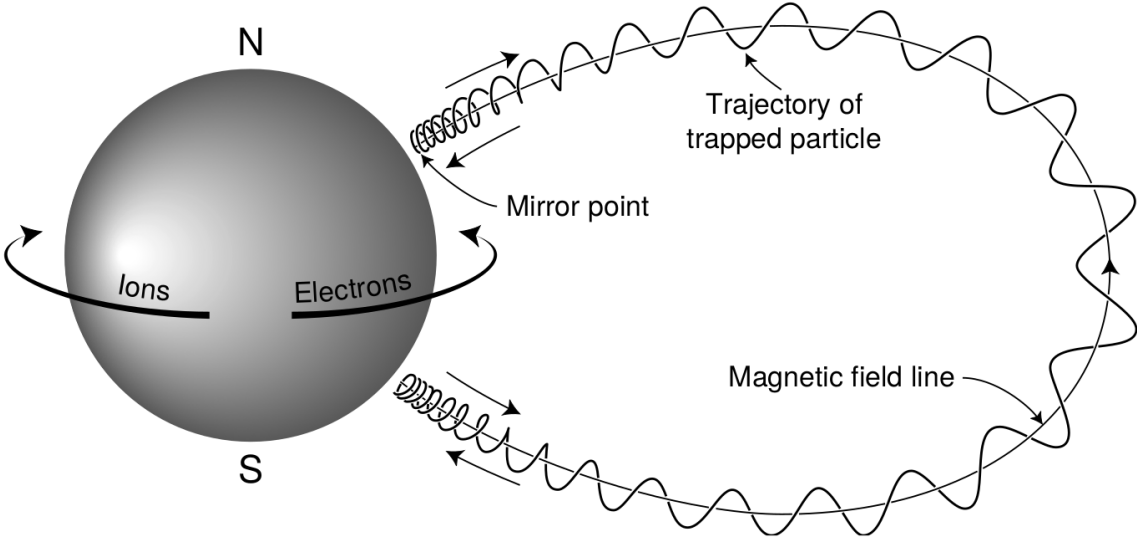


Figure 1.1: The three periodic motions of charged particles in Earth's dipole magnetic field. These motions are: gyration about the magnetic field line, bounce motion between the magnetic poles, and azimuthal drift around the Earth. Figure from (Baumjohann and Treumann, 1997).

magnitude B . This motion is circular with a Larmor radius of

$$r = \frac{mv_{\perp}}{|q|B} \quad (1.2)$$

where m is the mass and v_{\perp} the particle's velocity perpendicular to \vec{B} . This motion has a corresponding gyrofrequency

$$\Omega = \frac{|q|B}{m} \quad (1.3)$$

in units of radians/second. In the radiation belts, the electron gyrofrequency, Ω_e is on the order of a kHz. The corresponding adiabatic invariant is found by integrating the particle's canonical momentum around the particle's path of gyration

$$J_i = \oint (\vec{p} + q\vec{A}) \cdot d\vec{l} \quad (1.4)$$

42 where J_i is the i^{th} adiabatic invariant and \vec{A} is the magnetic vector potential. This
 43 integral is carried out by integrating the first term over the circumference of the
 44 gyro orbit and integrating the second term using Stokes theorem to calculate the
 45 magnetic flux enclosed by the gyro orbit. The gyration invariant is $J_1 \sim v_{\perp}^2/B$, which
 46 is conserved when the frequency, ω of a force acting on the gyrating electron satisfies
 47 $\omega \ll \Omega_e$.

48 The second highest frequency periodic motion is bouncing due to a parallel
 49 gradient in \vec{B} . This periodic motion naturally arises in the magnetosphere because
 50 Earth's magnetic field is stronger near the poles, and artificially in the laboratory
 51 in magnetic bottle machines. To understand this motion we first we need to define
 52 the concept of pitch angle, α as the angle between \vec{B} and \vec{v} which is schematically
 53 shown in Fig. 1.2a. The pitch angle relates v with v_{\perp} , and v_{\parallel} (the component of the
 54 particles velocity parallel to \vec{B}). As shown in Fig. 1.2b and 1.2c, a smaller (larger)
 55 α will increase (decrease) the distance that the charged particle travels parallel to \vec{B} ,
 56 during one gyration.

Assuming the particle's kinetic energy is conserved, the conservation of J_1
 implies that given a particle's $v_{\perp}(0)$ and $B(0)$ at the magnetic equator (where
 Earth's magnetic field is usually at a minimum), we can calculate its $v_{\perp}(s)$ along the
 particle's path s by calculating $B(s)$ from magnetic field models. Thus the particle's
 perpendicular velocity is then related via

$$\frac{v_{\perp}^2(0)}{B(0)} = \frac{v_{\perp}^2(s)}{B(s)} \quad (1.5)$$

57 which can be rewritten as

$$\frac{v^2 \sin^2 \alpha(0)}{B(0)} = \frac{v^2 - v_{\parallel}^2(s)}{B(s)} \quad (1.6)$$

⁵⁸ and re-arranged to solve for $v_{||}(s)$

$$v_{||}(s) = v \sqrt{1 - \frac{B(s)}{B(0)} \sin^2 \alpha(0)} \quad (1.7)$$

⁵⁹ which will tend towards 0 when the second term in the radical approaches 1.

⁶⁰ The location where $v_{||}(s) = 0$ is called the mirror point and is where a particle
⁶¹ reverses direction. Since Earth's magnetic field is stronger towards the poles, the
⁶² mirroring particle will execute periodic bounce motion between its two mirror points
⁶³ in the northern and southern hemispheres. The corresponding adiabatic invariant, J_2
⁶⁴ is

$$J_2 = \oint p_{||} ds \quad (1.8)$$

where ds describes the particle path between the mirror points in the northern and southern hemispheres (see Fig. 1.1). J_2 is found by substituting Eq. 1.7 into Eq. 1.8 and defining the magnetic field strength at the mirror points as B_m (where $\alpha(m) = 90^\circ$). The J_2 integral can be written as

$$J_2 = 2p \int_{m_n}^{m_s} \sqrt{1 - \frac{B(s)}{B(m)}} ds \quad (1.9)$$

⁶⁵ where m_n and m_s are the northern and southern mirror points, respectively. The
⁶⁶ bounce period can be estimated (e.g. Baumjohann and Treumann, 1997) to be

$$t_b \approx \frac{LR_e}{\sqrt{W/m}} (3.7 - 1.6 \sin \alpha(0)) \quad (1.10)$$

⁶⁷ where W is the particle's kinetic energy, and L is the L -shell. L -shell describes the
⁶⁸ distance from the Earth's center to the location where a particular magnetic field
⁶⁹ line crosses the magnetic equator, in units of Earth radii, R_e . As with gyration, the

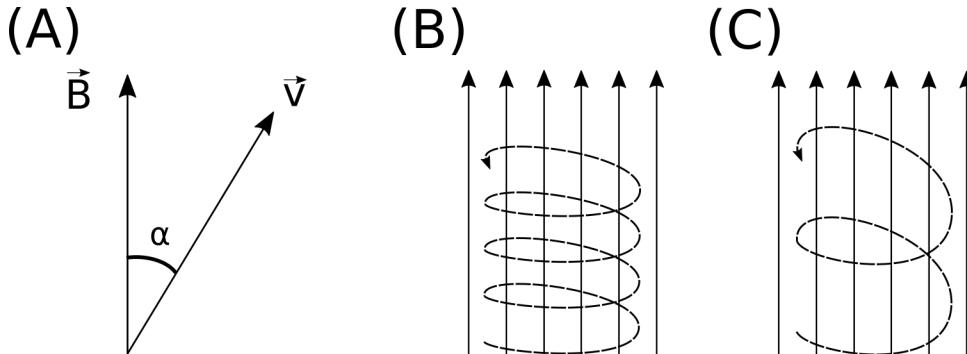


Figure 1.2: Charged particle motion in a uniform magnetic field \vec{B} . Panel (A) shows the geometry defining the pitch angle, α . Panel (B) and (C) show two helical electron trajectories with dashed lines assuming a large and small α (corresponding to a small and large parallel velocity $v_{||}$), respectively.

70 particle will bounce between the mirror points as long as $\omega \ll \Omega_b$, where Ω_b is the
71 bounce frequency.

72 At this stage it is instructional to introduce the notion of the loss cone pitch
73 angle, α_L . A particle with $\alpha \leq \alpha_L$ will mirror at or below ≈ 100 km altitude in
74 the atmosphere. A charged particle gyrating at those altitudes will encounter and
75 Coulomb scatter with the dense atmosphere and be lost from the magnetosphere.

76 The slowest periodic motion experienced by charged particles in Earth's mag-
77 netic field is azimuthal drift around the Earth. This drift results from a combination of
78 a radial gradient in \vec{B} and the curvature of the magnetic field. The radial gradient drift
79 arises because Earth's magnetic field is stronger near the Earth where the particle's
80 gyroradius radius of curvature shrinks as it gyrates towards stronger magnetic field,
81 and expands when it gyrates outward. The overall effect is the particle gyro orbit does
82 not close on itself and negatively charged particles drift east and positively charged
83 particles drift west. The radial gradient drift is further enhanced by the centrifugal
84 force that a particle experiences as it bounces along the curved field lines. The drift
85 adiabatic invariant, J_3 is found by integrating Eq. 1.4 over the complete particle orbit

86 around the Earth. The shape of this drift orbit is known as a drift shell. For J_3 , the
 87 first term is negligible and the second term is the magnetic flux enclosed by the drift
 88 shell, Φ_m i.e. $J_3 \sim \Phi_m$.

89 Figure 1.3 from Schulz and Lanzerotti (1974) shows contours of the gyration,
 90 bounce, and drift frequencies for electrons and protons in Earth's dipole magnetic
 91 field.

Up until now we have considered the three periodic motions due Earth's magnetic field in the absence of electric fields. If there is an electric field, E_\perp perpendicular to \vec{B} , a particle's center of gyration i.e., averaged position of the particle over a gyration, will drift with a velocity perpendicular to both E_\perp and \vec{B} . The drift velocity can be solved using Eq. 1.1 and is

$$\vec{v}_E = \frac{\vec{E} \times \vec{B}}{B^2}. \quad (1.11)$$

92 If there is a parallel magnetic field, $E_{||}$ then the particle is accelerated along the
 93 magnetic field line. An $E_{||}$ pointing away from the Earth will contribute to the mirror
 94 force and raise the particle's mirror point. On the contrary, an Earthward pointing
 95 $E_{||}$ will oppose the mirror force and lower the mirror point. If the Earthward $E_{||}$ is
 96 strong enough, the mirror point is lowered into the atmosphere that will precipitate
 97 particles. This is the mechanism that generates the aurora.

98 Particle Populations and Their Interractions in the Magnetosphere

99 Now that we have looked at the dynamics of single-particle motion in electric
 100 and magnetic fields, we will briefly tour the various macroscopic populations in the
 101 magnetosphere that are illustrated in Fig. 1.4.

102 The sun and its solar wind are ultimately the source of energy input into the
 103 magnetosphere. The solar wind at Earth's orbit is a plasma traveling at supersonic

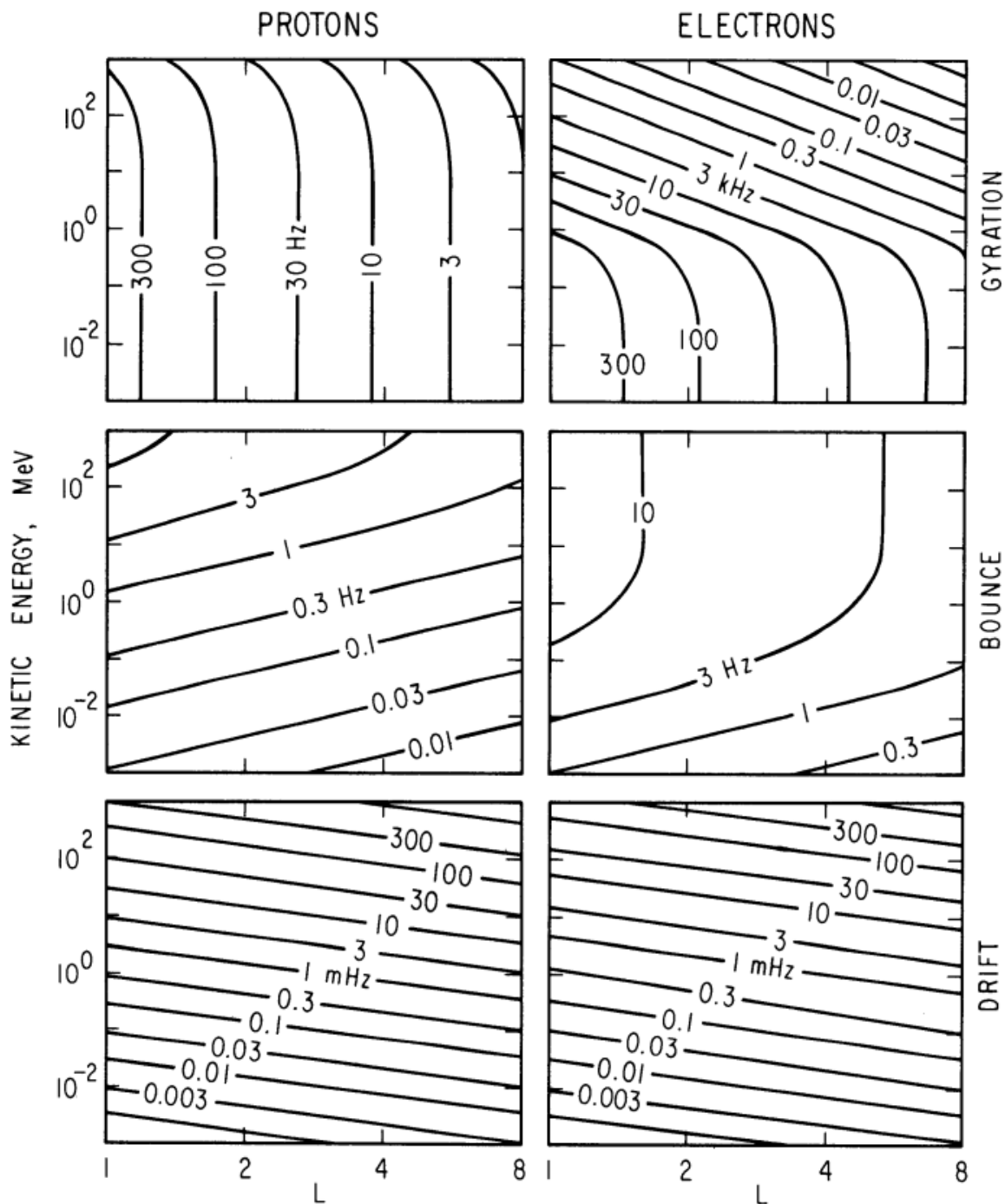


Figure 1.3: Contours of constant gyration, bounce, and drift frequencies for electrons and protons in a dipole field. Figure from Schulz and Lanzerotti (1974).

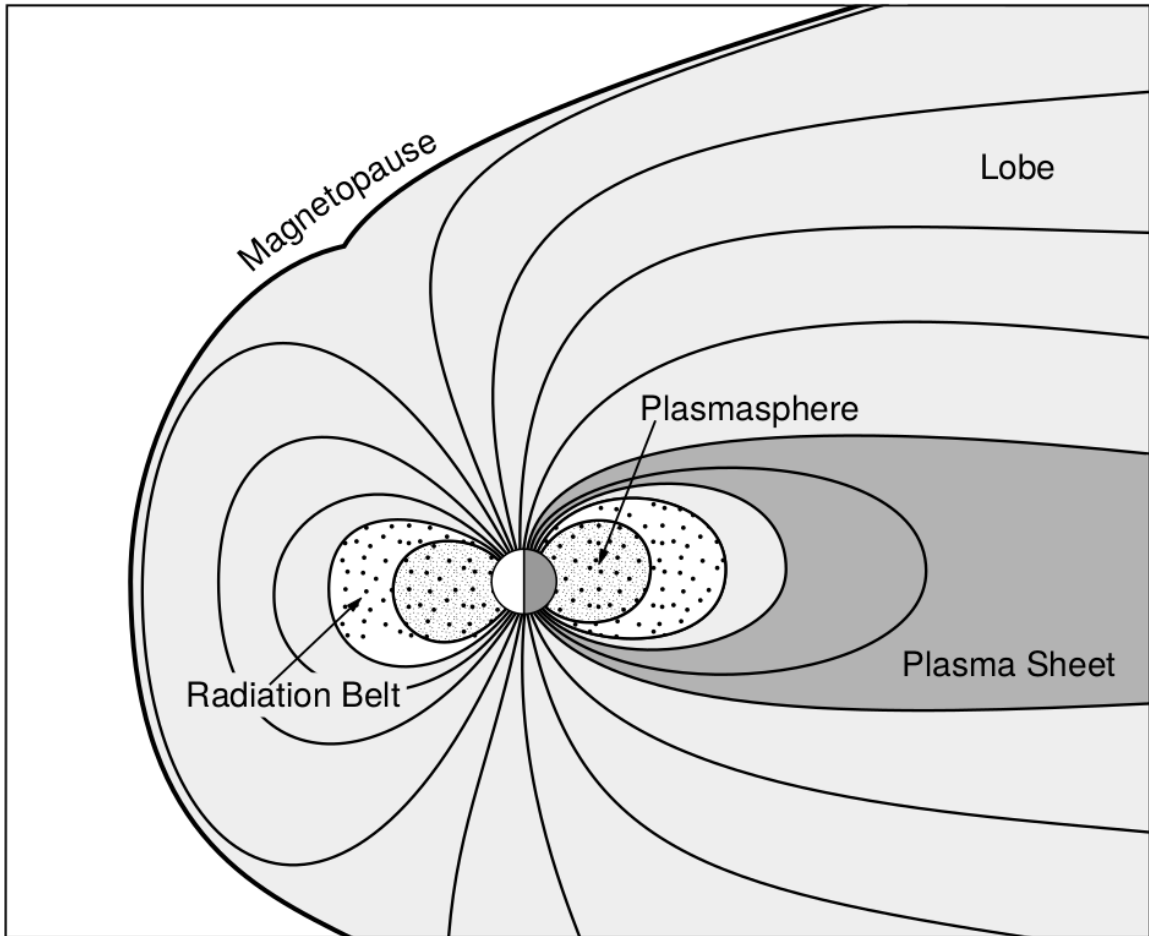


Figure 1.4: A few macroscopic structures in the magnetosphere. The magnetosphere boundary with the solar wind is the magnetopause. The magnetotail consists of two lobes that contain Earth's magnetic flux with the plasma sheet separating the two lobes. The inner magnetosphere contains the plasmasphere, the ring current, and the radiation belts which are co-located. Figure from Baumjohann and Treumann (1997).

speeds with an embedded interplanetary magnetic field (IMF). When the solar wind encounters Earth's magnetic field, the plasma can not easily penetrate into the magnetosphere because the plasma is frozen-in on magnetic field lines. Thus the plasma and its magnetic field drapes around the magnetosphere, forming a cavity in the solar wind that qualitatively has a shape as shown in Fig. 1.4. Because the solar wind is supersonic at 1 AU, a bow shock exists upstream of the magnetosphere. The solar wind plasma, after it is shocked by the bow shock, flows around the magnetosphere inside the magnetosheath. The surface where the solar wind ram pressure and Earth's magnetic pressure balance is termed the magnetopause, which can be thought of as a boundary between the solar wind and Earth's magnetosphere. This is a slightly naive description of the magnetopause, but is nonetheless an instructive conceptual picture. The shocked plasma then flows past the Earth where it shapes the magnetotail. In the magnetotail the magnetopause exists where the solar wind magnetic pressure balances Earth's magnetic field pressure in the lobes. The magnetotail extends on the order of $100 R_E$ downstream of Earth, and the tailward stretching of magnetic field lines creates the plasma sheet which exists in the region of low magnetic field strength near the magnetic equator (e.g. Eastwood et al., 2015).

121 Populations in the Inner Magnetosphere

Closer to Earth, where the magnetic field is largely dipolar, are three plasma populations that comprise the inner magnetosphere: the plasmasphere, the ring current, and the radiation belts which are shown in Fig. 1.4. Before we describe these three particle populations in detail, we will first introduce the coordinate system that most naturally describes the inner magnetosphere environment, and then the electric fields that effect mostly low energy particles.

In this coordinate system the “radial” coordinate was defined in section 1 and

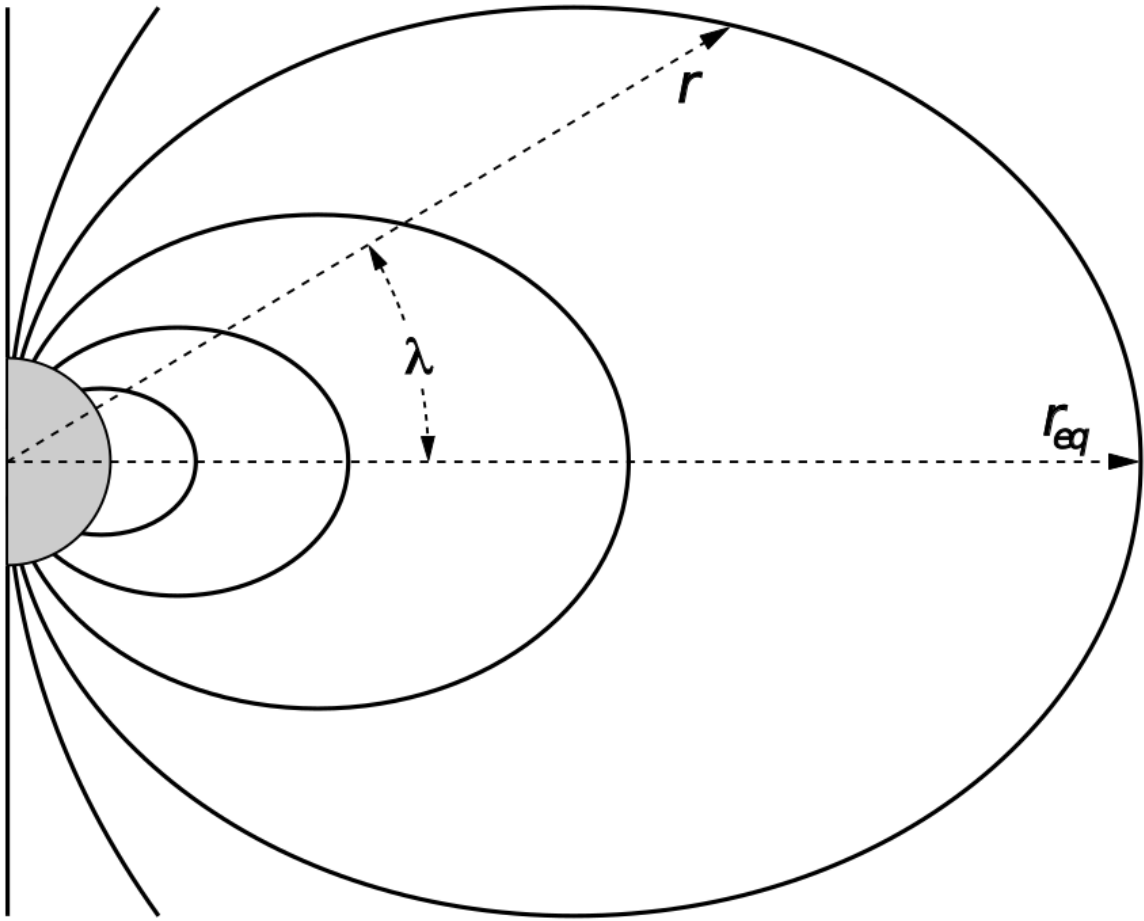


Figure 1.5: The dipole coordinate system. The magnetic latitude of \mathbf{r} is λ . The radial distance to a magnetic field line in the equatorial plane is typically given by $L = r_{eq}/R_e$. Figure from Baumjohann and Treumann (1997).

is the L shell. The azimuthal coordinate is the magnetic local time (MLT). For an observer above Earth's north pole looking down, MLT is defined to be 0 (midnight) in the anti-sunward direction, and increases in the counter-clockwise direction with 6 at dawn, 12 at noon (sunward direction), and 18 in dusk. The final coordinate is the magnetic latitude, λ which is analogous to the latitude coordinate in the spherical coordinate system, and is defined to be 0 at the magnetic equator. This coordinate system is shown in Fig. 1.5 and naturally describes the inner magnetosphere populations described below.

137 The low energy particle dynamics in the inner magnetosphere are organized by
 138 two electric fields: the co-rotation and the dawn-dusk electric fields. The co-rotation
 139 electric field arises from Earth's rotation. The magnetic field and the particles frozen
 140 on it rotate with the Earth. To a non-rotating observer this rotation appears as a
 141 radial electric field that drops off as $\sim L^{-2}$. The other electric field, pointing from
 142 dawn to dusk is called the convection electric field and is due to the Earthward
 143 transport of particles from the magnetotail that appears as an electric field in Earth's
 144 reference frame. The superposition of the co-rotation and convection electric
 145 fields is a potential field shown in Fig. 1.6. The shaded area in Fig. 1.6 shows the
 146 orbits on which low energy electrons are trapped, and outside this region the particles
 147 are not trapped. The dynamic topology of the shaded region in Fig. 1.6 is controlled
 148 by only the convection electric field which is dependent on the solar wind speed and
 149 the IMF. The lowest energy particles that orbit in the shaded region in Fig. 1.6 make
 150 up the plasmasphere.

151 Plasmasphere The plasmasphere is a dense ($n_e \sim 10^3/\text{cm}^3$), cool ($\sim \text{eV}$)
 152 plasma. The plasmasphere typically extends to $L \sim 4$ and the spatial extent is
 153 highly dependent on the solar wind and magnetospheric conditions. The source
 154 of the plasmasphere is the ionosphere. The two main mechanisms that fill the
 155 plasmasphere with cold plasma are ionization of the ionosphere by sunlight and
 156 particle precipitation. The ultraviolet ionization by sunlight is strongly dependent
 157 on the time of day (day vs night), latitude (more ionization near the equator). The
 158 ionization due to particle precipitation, on the other hand, is highly dependent on
 159 magnetospheric conditions, and mostly occurs at high latitudes.

160 The outer boundary of the plasmasphere is the plasmapause which is typically
 161 identified as a steep radial gradient in plasma density from $\sim 10^3/\text{cm}^3$ to $\sim 1/\text{cm}^3$.

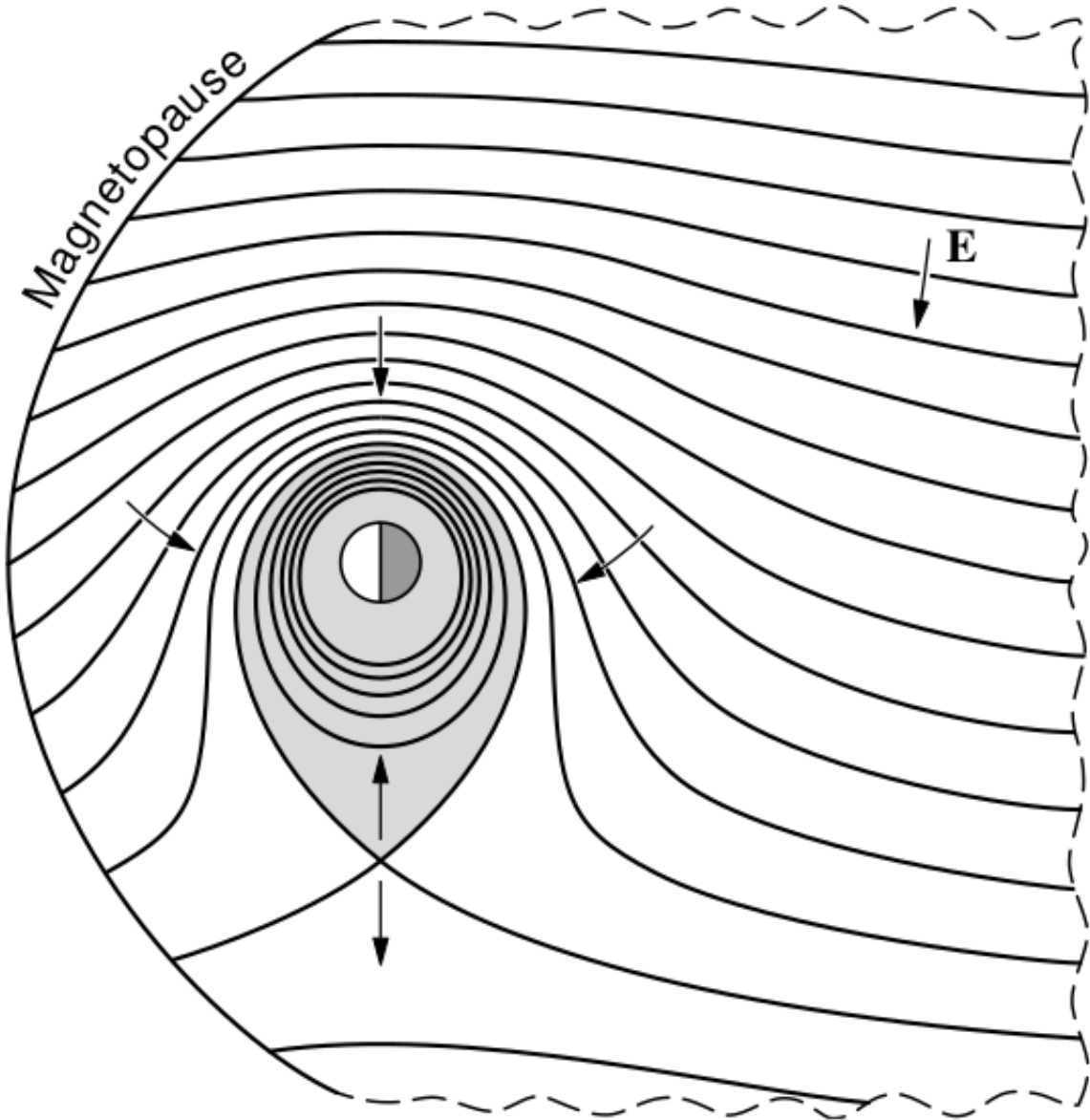


Figure 1.6: Equipotential lines and electric field arrows due to the superposition of the co-rotation and convection electric fields. Electrons in the shaded region execute closed orbits. Outside of the shaded regions the electrons are not trapped and will escape. The region separating the two regimes is called the Alfvén layer. Figure from Baumjohann and Treumann (1997).

₁₆₂ The location of the plasmapause is important to model (e.g. O'Brien and Moldwin,
₁₆₃ 2003) and understand since the plasma density strongly controls the efficiency of
₁₆₄ particle scattering by waves (e.g. Horne et al., 2005).

₁₆₅ Ring Current The next higher energy population is the ring current. This
₁₆₆ population consists of protons and electrons between tens and a few hundred keV
₁₆₇ that drift around the Earth. The orbits of higher energy particles are not as effected
₁₆₈ by the convection and co-rotation electric field, rather they drift around the Earth
₁₆₉ due to gradient and curvature drifts. Since the direction of the drift is dependent on
₁₇₀ charge, protons drift west around the Earth and electrons drift East. This has the
₁₇₁ effect of creating a current around the Earth.

₁₇₂ The ring current generates a magnetic field which decreases the magnetic field
₁₇₃ strength at the surface of the Earth and increases it outside of the ring current.
₁₇₄ The decrease of Earth's magnetic field strength is readily observed by a system of
₁₇₅ ground-based magnetometers and is merged into a Disturbance Storm Time (DST)
₁₇₆ index to quantify the global reduction in the magnetic field. An example of a DST
₁₇₇ index time series from the 2015 St. Patrick's Day storm, driven by a coronal mass
₁₇₈ ejection (CME), is shown in Fig. 1.7. A few notable features of the storm and the
₁₇₉ ring current are worth pointing out. At the start of the storm the ring current is
₁₈₀ sometimes depleted and DST increases slightly (termed the initial phase or sudden
₁₈₁ storm commencement). Then the ring current population is rapidly built up and
₁₈₂ DST rapidly decreases during the main phase. Lastly, after the storm passes, the
₁₈₃ ring current gradually decays toward its equilibrium state over a period of a few
₁₈₄ days and DST returns towards 0 during the recovery phase. The DST index (along
₁₈₅ with other geomagnetic indices) are readily used by the space physics community to
₁₈₆ quantify the global state of the magnetosphere.

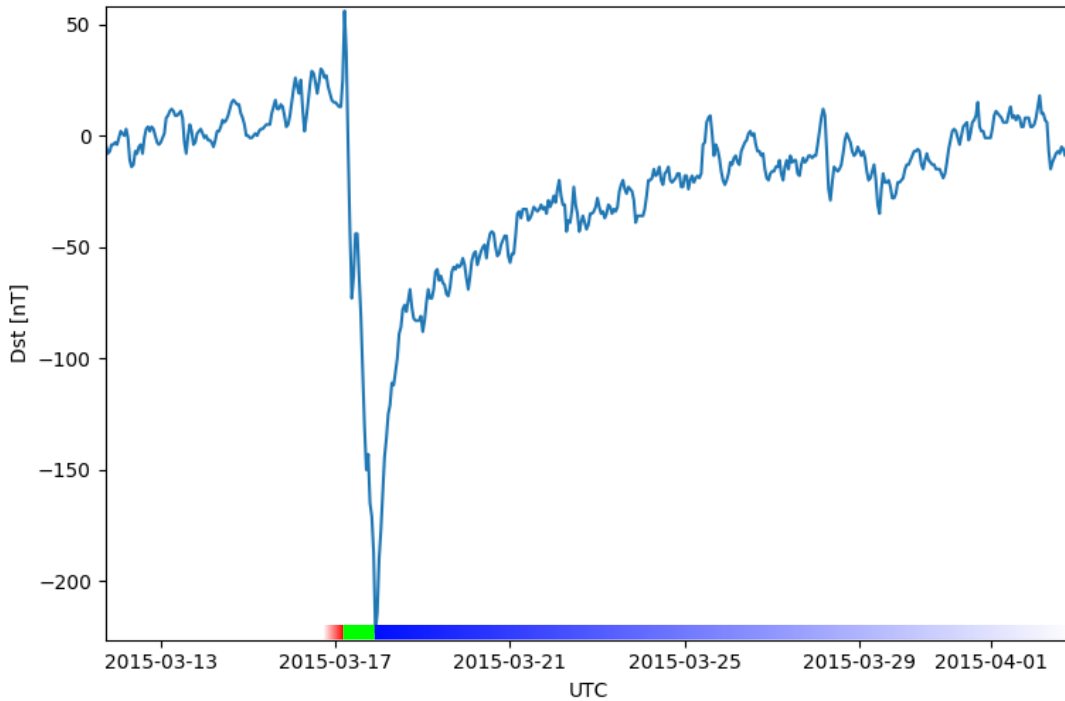


Figure 1.7: The DST index during the St. Patrick's Day 2015 storm. This storm was caused by a coronal mass ejection on March 15th, 2015. The storm phases are: initial phase, main phase, and recovery phase. The initial phase occurred when the Dst peaked at +50 nT on March 17th during which the ring current was eroded by the coronal mass ejection during the interval shown by the red bar shown at the bottom. Then the following rapid decrease to ≈ -200 nT was during the main phase where many injections from the magnetotail enhanced the ring current, which reduced Earth's magnetic field strength at the ground, and is shown with the green bar. Lastly, the recovery phase lasted from March 18th to approximately March 29th during which the ring current particles were lost and the ring current returned to its equilibrium state. The recovery phase is shown with the blue bar.

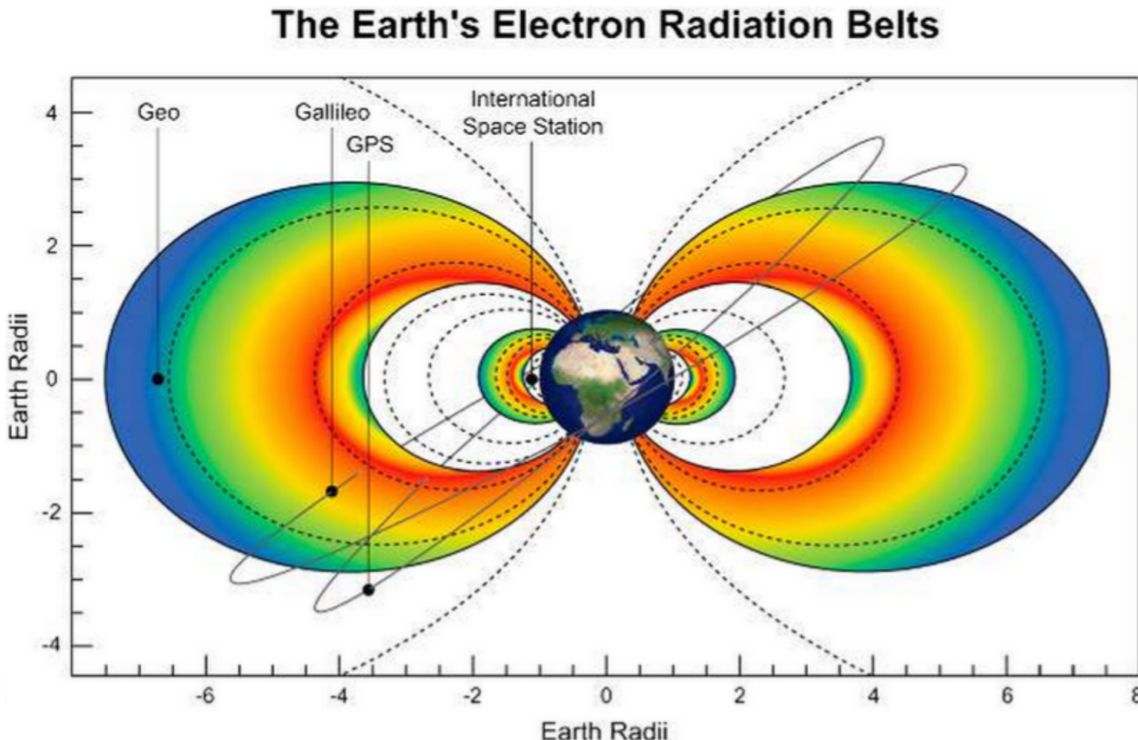


Figure 1.8: The two radiation belts with the locations of various satellites and orbits. Figure from (Horne et al., 2013).

187 Radiation Belts The highest particle energy populations are in the Van Allen
 188 radiation belts. These belts were discovered by Van Allen (1959) and Vernov and
 189 Chudakov (1960) during the Cold War and are a pair of toroidally shaped populations
 190 of trapped electrons and protons shown in Fig. 1.8. Their quiescent toroidal shape,
 191 similar to the shape of the plasmasphere and ring current, is a result of Earth's dipole
 192 magnetic field.

193 The inner radiation belt is extremely stable on time periods of years, extends
 194 to $L \approx 2$, and mainly consists of protons with energies between MeV and GeV and
 195 electrons with energies up to ≈ 1 MeV (Claudepierre et al., 2019). The source of
 196 inner radiation belt protons is believed to be due to cosmic-ray albedo neutron decay
 197 (e.g. Li et al., 2017) and inward radial diffusion for electrons (e.g. O'Brien et al.,

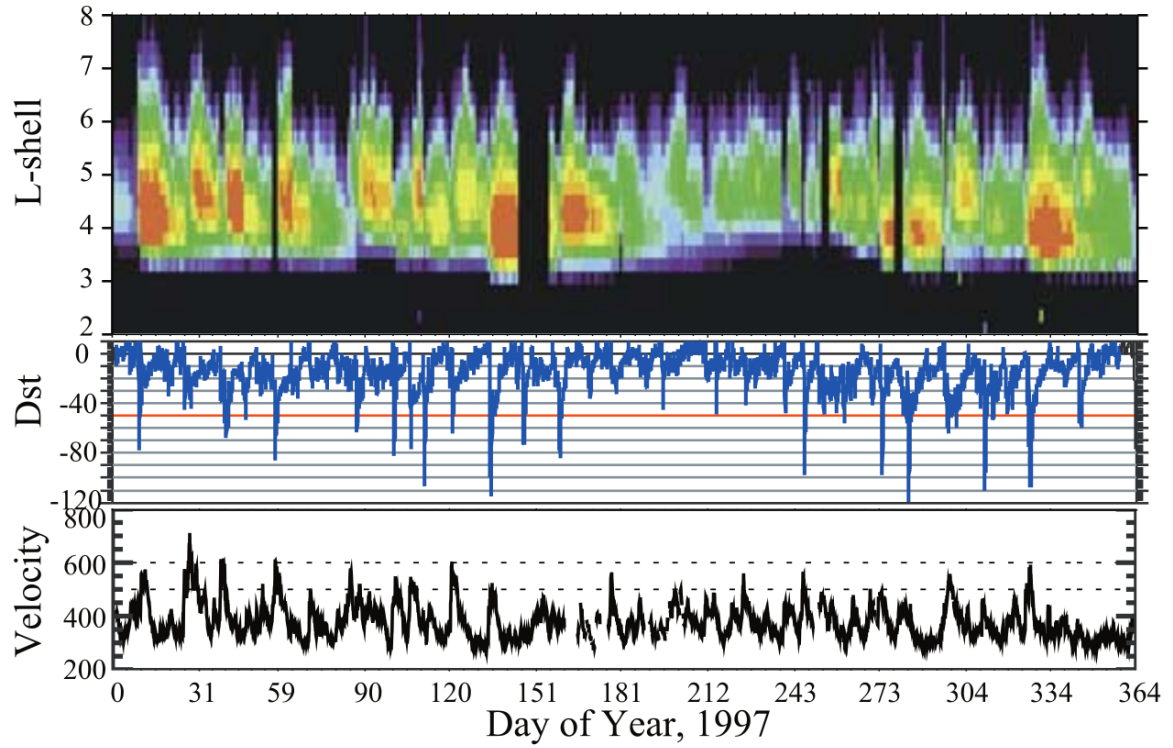


Figure 1.9: The dynamics of the outer radiation belt in 1997 from the POLAR satellite. Top panel shows the 1.2-2.4 MeV electron flux as a function of L and 1997 day of year. The middle panel shows the DST index, and bottom panel shows the solar wind velocity. Figure from (Reeves et al., 2003).

¹⁹⁸ 2016). The gap between the inner and outer radiation belt is called the slot, which is
¹⁹⁹ believed to be due to hiss waves inside the plasmasphere (described below) scattering
²⁰⁰ particles into the atmosphere (e.g. Breneman et al., 2015; Lyons and Thorne, 1973).

²⁰¹ The outer radiation belt is much more dynamic and consists of mainly electrons
²⁰² of energies up to a few MeV. The outer belt's spatial extent is highly variable as
²⁰³ shown in Fig. 1.9, and is typically observed between L of 4 and 8. The source of
²⁰⁴ outer radiation belt electrons is widely believed to be injections of plasma from the
²⁰⁵ magnetotail that is then accelerated to high energies.

²⁰⁶ Due to the highly energetic and dynamic nature of the radiation belts, and their
²⁰⁷ impact on human presence in space, the radiation belts have been studied for over
²⁰⁸ half century. Researchers have studied and attempted to predict the dynamics of
²⁰⁹ radiation belt particles, waves, and wave-particle interactions by considering various
²¹⁰ competing particle acceleration and loss mechanisms which are described next.

²¹¹ Radiation Belt Particle Sources and Sinks

²¹² Adiabatic Heating

²¹³ One of the particle heating and transport mechanisms arises from the Earthward
²¹⁴ convection of particles. The conservation of J_1 implies that the initial and final v_\perp
²¹⁵ depends on the change in the magnetic field amplitude

$$\frac{v_{\perp i}^2}{B_i} = \frac{v_{\perp f}^2}{B_f}. \quad (1.12)$$

²¹⁶ As a particle convects Earthward, $B_f > B_i$ thus v_\perp must increase. The dipole
²¹⁷ magnetic field amplitude can be written as

$$B(L, \theta) = \frac{31.2 \mu\text{T}}{L^3} \sqrt{1 + 3 \cos^2 \theta}. \quad (1.13)$$

₂₁₈ The change in v_{\perp}^2 can be found by taking the ratio of $B(L, \theta)$ at two different L shells

$$\frac{v_{\perp f}^2}{v_{\perp i}^2} = \left(\frac{L_i}{L_f} \right)^3 \quad (1.14)$$

₂₁₉ thus the increase in $v_{\perp} \sim (L_i/L_f)^{3/2}$.

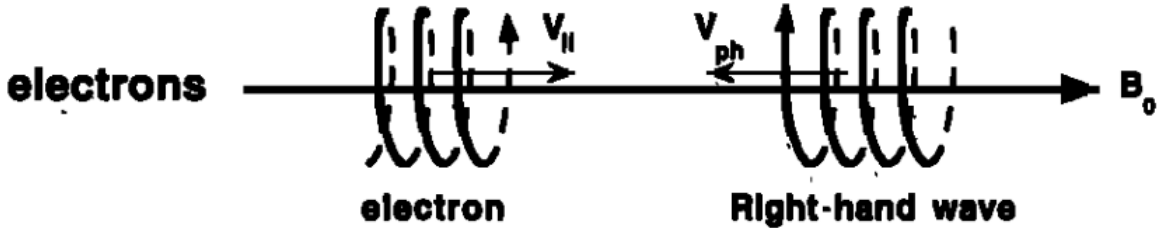
₂₂₀ As the particle convects Earthward its v_{\parallel} also increases because the distance
₂₂₁ between the particle's mirror points decrease. If J_2 is conserved, the shrinking bounce
₂₂₂ path implies that v_{\parallel} must increase by

$$\frac{v_{\parallel f}^2}{v_{\parallel i}^2} = \left(\frac{L_i}{L_f} \right)^k \quad (1.15)$$

₂₂₃ where k ranges from 2 for equatorial pitch angles, $\alpha_{eq} = 0^\circ$, to 2.5 for $\alpha_{eq} = 90^\circ$
₂₂₄ (Baumjohann and Treumann, 1997). Since the rate of adiabatic heating is greater in
₂₂₅ the perpendicular direction than heating in the parallel direction, an initially isotropic
₂₂₆ particle distribution will become anisotropic during its convection. These isotropic
₂₂₇ particles can then become unstable to wave growth and generate waves in order to
₂₂₈ reach equilibrium.

₂₂₉ Wave Resonance Heating

₂₃₀ Another mechanism that heats particles is due to particles resonating with
₂₃₁ plasma waves. A few of the electromagnetic wave modes responsible for particle
₂₃₂ acceleration (and scattering) relevant to radiation belt dynamics are hiss, whistler
₂₃₃ mode chorus (chorus), and electromagnetic ion cyclotron (EMIC) waves. These waves
₂₃₄ are created by the loss cone instability that is driven by an anisotropy of electrons for
₂₃₅ chorus waves, and protons for EMIC waves. The level of anisotropy can be quantified
₂₃₆ by the ratio of the perpendicular to parallel particle temperatures (T_{\perp}/T_{\parallel}). A particle
₂₃₇ distribution is unstable when $T_{\perp}/T_{\parallel} > 1$. Since electrons gyrate in a right-handed



$$\omega + k_{\parallel} v_{\parallel} = \Omega^-$$

Figure 1.10: The trajectories of an electron and a right-hand circularly polarized wave during a cyclotron resonance. The electron's v_{\parallel} and the wave's k_{\parallel} are in opposite directions such that the wave's frequency is Doppler shifted to an integer multiple of the electron cyclotron frequency. Figure from (Tsurutani and Lakhina, 1997).

²³⁸ sense, the chorus waves also tend to be right hand circularly polarized (Tsurutani and
²³⁹ Lakhina, 1997). The same argument also applies to protons and left hand circularly
²⁴⁰ polarized EMIC waves.

²⁴¹ These circularly polarized waves can resonate with electrons and/or protons
²⁴² when their relative motion results in a static \vec{E} . One example of a resonance between
²⁴³ a right hand circularly polarized wave and an electron is shown in Fig. 1.10. The
²⁴⁴ electron's v_{\parallel} and the wave's parallel wave vector, k_{\parallel} are in opposite directions such
²⁴⁵ that the wave frequency ω is Doppler shifted to an integer multiple of the Ω_e where the
²⁴⁶ electron feels a static electric field and is accelerated or decelerated. Quantitatively,
²⁴⁷ this resonance condition is easier to understand with the following toy model.

²⁴⁸ Assume a uniform magnetic field $\vec{B} = B_0 \hat{z}$ with a parallel propagating ($k = k \hat{z}$),
²⁴⁹ right-hand circularly polarized wave. The wave's electric field as a function of position
²⁵⁰ and time can be written as

$$\vec{E} = E_0(\cos(\omega t - kz)\hat{x} + \sin(\omega t - kz)\hat{y}). \quad (1.16)$$

The angular component of \vec{E} that will effect the particle's v_{\perp} is

$$E_{\theta} = \vec{E} \cdot \hat{\theta} = E_0 \cos(\omega t - kz + \theta). \quad (1.17)$$

²⁵¹ Now assume that the electron is traveling in the $-\hat{z}$ direction with a velocity $\vec{v} = -v_0 \hat{z}$

²⁵² so its time dependent position along \hat{z} is

$$z(t) = -v_0 t \quad (1.18)$$

²⁵³ and gyrophase is

$$\theta(t) = -\Omega t + \theta(0) \quad (1.19)$$

²⁵⁴ where the first negative sign comes from the electron's negative charge. Now we put
²⁵⁵ this all together and find the force that the electron will experience

$$m \frac{dv_{\theta}}{dt} = q E_{\theta} = q E_0 \sin((\omega + kv_0 - \Omega)t + \theta(0)). \quad (1.20)$$

²⁵⁶ This is a relatively complex expression, but when the time dependent component is
²⁵⁷ 0, i.e.

$$\omega + kv_0 - \Omega = 0, \quad (1.21)$$

²⁵⁸ the electron will feel a static electric field and be accelerated or decelerated depending
²⁵⁹ on θ_0 , the phase between the wave and the electron. The expression in Eq. 1.21 is
²⁶⁰ commonly referred to as the resonance condition and is more generally written as

$$\omega - k_{||} v_{||} = \frac{n \Omega_e}{\gamma} \quad (1.22)$$

261 where n is the resonance order, and γ is the relativistic correction (e.g. Millan and
 262 Thorne, 2007). In the case of the cyclotron resonance, $\omega \approx \Omega_e$ thus J_1 is violated.
 263 Since J_1 is violated, J_2 and J_3 are also violated since the conditions required to
 264 violate J_2 and J_3 are less stringent than J_1 . It is important to remember that along
 265 the particle's orbit it will encounter and experience the effects of many waves along
 266 its orbit. The typical MLT extent of a handful of waves that are capable of resonating
 267 with radiation belt electrons are shown in Fig. 1.11.

268 Particle Losses

269 Now that we have seen two general mechanisms with which particles are
 270 accelerated and transported in the magnetosphere, we will now consider a few
 271 specific mechanisms with which particles are lost to the atmosphere or the solar
 272 wind. One particle loss mechanism into the solar wind is magnetopause shadowing
 273 (e.g. Ukhorskiy et al., 2006). Particles are sometimes lost when the ring current is
 274 strengthened and Earth's magnetic field strength is increased outside of the ring
 275 current (and reduced on Earth's surface). If the time scale of the ring current
 276 strengthening is slower than a particle drift, J_3 is conserved. Then in order to
 277 conserve J_3 while the magnetic field strength is increased, the particle's drift shell
 278 must move outward to conserve the magnetic flux contained by the drift shell. Then
 279 if the particle's drift shell expands to the point that it crosses the magnetopause, the
 280 particle will be lost to the solar wind.

281 Another particle loss (and acceleration) mechanism is driven by ultra low
 282 frequency (ULF) waves and is called radial diffusion. Radial diffusion is the transport
 283 of particles from high to low phase space density, f . If the transport is radially inward,
 284 particles will appear to be accelerated. On the other hand, radially outward radial
 285 diffusion can transport particles through the magnetopause where they will be lost

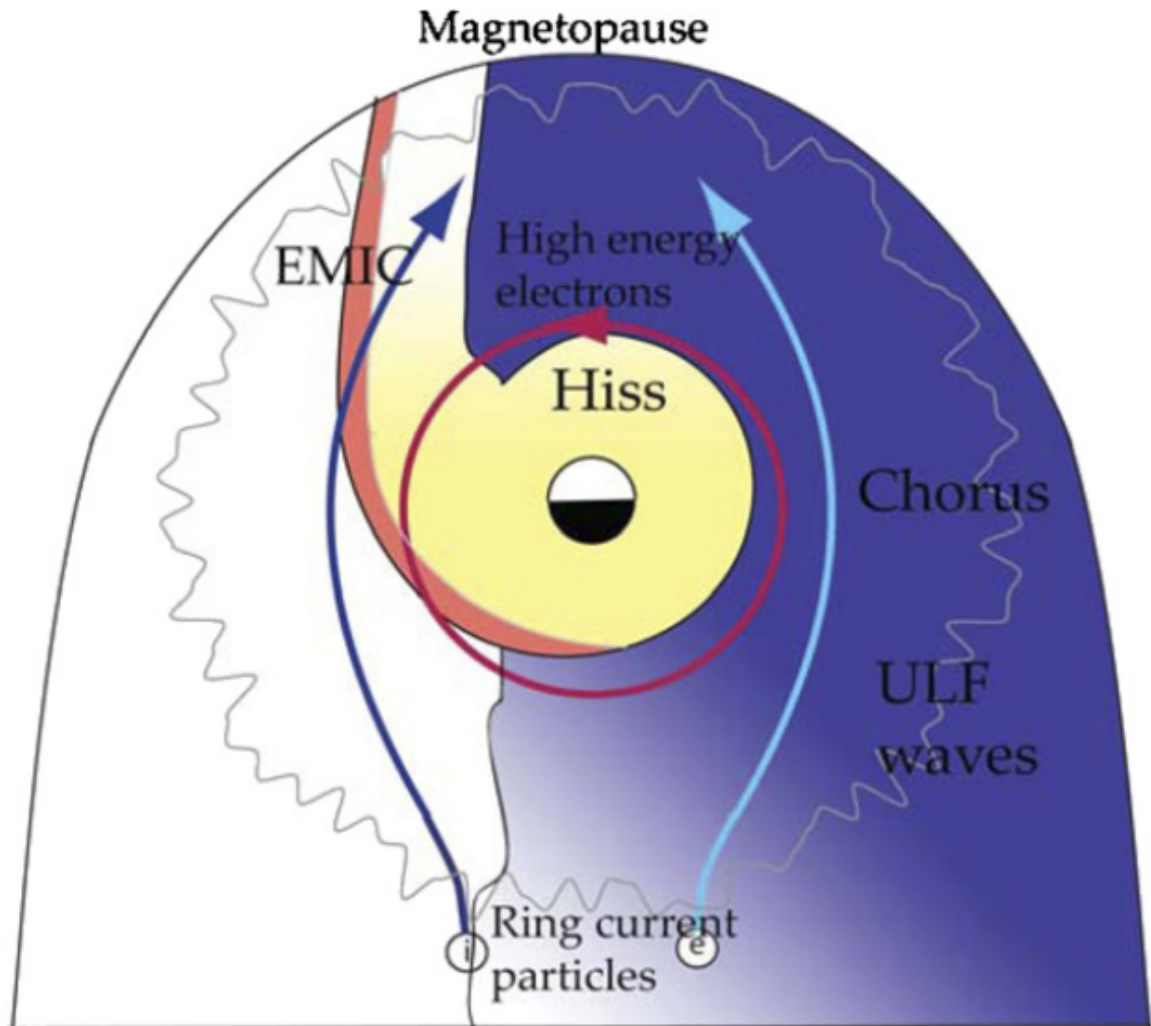


Figure 1.11: Various wave modes in the magnetosphere. Ultra low frequency waves occur through the magnetosphere. Chorus waves are typically observed in the 0-12 midnight-dawn region. EMIC waves are typically observed in the dusk MLT sector. Hiss waves are observed inside the plasmasphere. Figure from Millan and Thorne (2007).

286 to the solar wind. Reeves et al. (2013) investigated the driver of particle acceleration
 287 during the October 2012 storm and observationally found that inward radial diffusion
 288 was not dominant, rather local acceleration via wave-resonance heating (i.e. particle
 289 diffusion in pitch angle and energy which will be described below) appeared to be the
 290 dominant acceleration mechanism.

291 The loss mechanism central to this dissertation is pitch angle and energy
 292 scattering of electrons by waves. Some of the waves that scatter electrons in energy
 293 and pitch angle in the inner magnetosphere are: plasmaspheric hiss (e.g. Breneman
 294 et al., 2015; O'Brien et al., 2014), EMIC waves (e.g. Capannolo et al., 2019; Hendry
 295 et al., 2017), and chorus waves (e.g. Breneman et al., 2017; Kasahara et al., 2018;
 296 Ozaki et al., 2019). These wave-particle interactions occur when the resonance
 297 condition in Eq. 1.22 is satisfied at which point the particle's energy and α is modified
 298 by the wave. More details regarding the theory of pitch angle and energy diffusion
 299 is given in Chapter ???. If the wave changes α towards 0 such that $\alpha < \alpha_{LC}$, the
 300 particle's mirror point lowers to less than 100 km altitude where the particle can be
 301 lost due collisions with air. One manifestation of pitch angle scattering of particles
 302 into the loss cone are microbursts: a sub-second duraion impulse of electrons.

303

Microbursts

304 Microbursts were first found in high altitude balloon measurements of bremsstrahlung
 305 X-rays emitted by microburst electrons impacting the atmosphere by Anderson
 306 and Milton (1964). In the following years, numerous balloon flights expanded our
 307 knowledge of non-relativistic microbursts (relativistic microbursts have not yet been
 308 observed by high altitude balloons) by quantifying the microburst spatial extent,
 309 temporal width, occurrence frequency, extent in L and MLT, and their source (a
 310 local plasma instability vs. a propagating disturbance in the magnetosphere) (e.g.

311 Barcus et al., 1966; Brown et al., 1965; Parks, 1967; Trefall et al., 1966). Since then,
 312 non-relativistic and relativistic (> 500 keV) microbursts electrons have been directly
 313 observed in LEO with spacecraft including the Solar Anomalous and Magnetospheric
 314 Particle Explorer (SAMPEX) (e.g. Blake et al., 1996; Blum et al., 2015; Douma et al.,
 315 2019, 2017; Greeley et al., 2019; Lorentzen et al., 2001a,b; Nakamura et al., 1995, 2000;
 316 O'Brien et al., 2004, 2003), Montana State University's (MSU) Focused Investigation
 317 of Relativistic Electron Bursts: Intensity, Range, and Dynamics II (FIREBIRD-II)
 318 (Anderson et al., 2017; Breneman et al., 2017; Crew et al., 2016; Klumpar et al.,
 319 2015; Spence et al., 2012), and Science Technologies Satellite (STSAT-I) (e.g. Lee
 320 et al., 2012, 2005). An example microburst time series is shown in Fig. 1.12 and was
 321 observed by the FIREBIRD-II CubeSats. The prominent features of the example
 322 microbursts in Fig. 1.12 are their < 1 second duration, half order of magnitude
 323 increase in count rate above the falling background, and their approximately 200-800
 324 keV energy extent.

325 Microbursts are observed on magnetic field footprints that are connected to the
 326 outer radiation belt (approximately $4 < L < 8$), and are predominately observed in
 327 the 0-12 MLT sector with an elevated occurrence frequency during magnetospherically
 328 disturbed times as shown in Fig. 1.13 (e.g. Douma et al., 2017). O'Brien et al. (2003)
 329 used SAMPEX relativistic electron data and found that microbursts predominately
 330 occur during the main phase of storms, with a heightened occurrence rate during the
 331 recovery phase. Microburst occurrence rates also appear to be higher during high
 332 solar wind velocity events e.g. from co-rotating interaction regions (Greeley et al.,
 333 2019; O'Brien et al., 2003).

334 The impact of microbursts on atmospheric chemistry has been estimated to be
 335 significant. Relativistic microburst electrons impacting the atmosphere are ionized at
 336 < 100 km altitudes, with higher energy electrons penetrating closer to the surface.

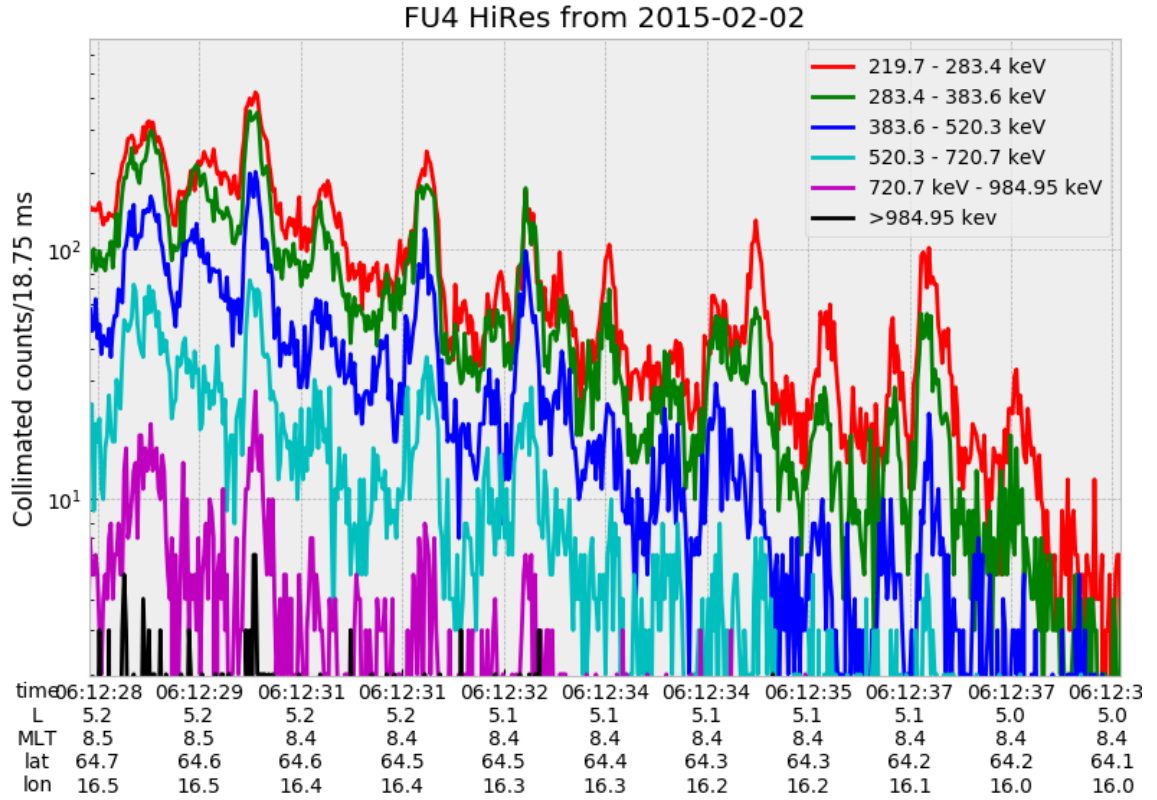


Figure 1.12: An example train of microbursts observed by FIREBIRD-II unit 4 on February 2nd, 2015. The colored curves show the differential energy channel count rates in six channels from ≈ 200 keV to greater than 1 MeV. The x-axis labels show auxiliary information such as time of observation and the spacecraft position in L, MLT, latitude and longitude coordinates.

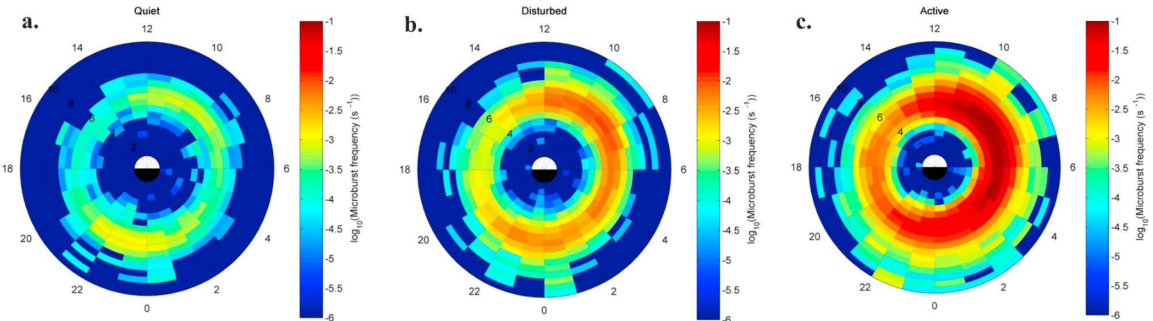


Figure 1.13: Relativistic ($> 1\text{MeV}$) distribution of microburst occurrence rates as a function of L and MLT. The three panels show the microburst occurrence rate dependence on geomagnetic activity, parameterized by the auroral electrojet (AE) index for (a) $\text{AE} < 100 \text{nT}$, (b) $100 < \text{AE} < 300 \text{nT}$ and (c) $\text{AE} > 300 \text{nT}$. Figure from Douma et al. (2017).

337 The resulting chemical reaction of microburst electrons impacting the atmosphere
 338 produces odd hydrogen HO_x and odd nitrogen NO_x molecules. These molecules are
 339 partially responsible for destroying ozone (O_3). Seppälä et al. (2018) modeled a six
 340 hour relativistic microburst storm and found that the mesospheric ozone was reduced
 341 by 7 – 12% in the summer months and 12 – 20% in the winter months.

342 Furthermore, microbursts have also been estimated to have a significant impact
 343 on the outer radiation belt electrons. Radiation belt electron loss due to microbursts
 344 has been estimated to be on the order of a day (Breneman et al., 2017; Douma
 345 et al., 2019; Lorentzen et al., 2001b; O’Brien et al., 2004; Thorne et al., 2005).

346 The wave-particle interactions responsible for generating microbursts are also
 347 believed to accelerate electrons in the radiation belts. As mentioned earlier, when
 348 an electron is in resonance with a wave, energy is exchanged with the wave and
 349 the electron is either accelerated or decelerated. The signature of wave-particle
 350 acceleration been observed for radiation belt electrons (e.g. Horne et al., 2005;
 351 Meredith et al., 2002; Reeves et al., 2013). O’Brien et al. (2003) presented evidence
 352 that enhancements in chorus waves, microbursts, and radiation belt electrons are

related. O'Brien et al. (2003) proposed an explanation where microburst precipitation is a side effect of electron acceleration due to chorus waves. The widely used theoretical framework to model interactions between electrons and chorus waves is quasi-linear diffusion (e.g. Horne et al., 2005; Meredith et al., 2002; Summers, 2005; Summers et al., 1998; Thorne et al., 2005; Walker, 1993) which is derived in Chapter ???. Qualitatively, when a particle is resonant with a wave it can be transported in pitch angle towards the loss cone and lose energy to the wave. In contrast, if the particle is transported away from the loss cone, it gains energy from the wave.

The range of observed microburst energies range from a few tens of keV (e.g Datta et al., 1997; Parks, 1967) to greater than 1 MeV (e.g. Blake et al., 1996; Greeley et al., 2019). The microburst electron flux (J) falls off in energy, and the microburst energy spectra is typically well fit to a decaying exponential

$$J(E) = J_0 e^{-E/E_0} \quad (1.23)$$

where J_0 is the flux at 0 keV (unphysical free parameter) and E_0 quantifies the efficiency of the scattering mechanism in energy (.e.g Datta et al., 1997; Lee et al., 2005; Parks, 1967). A small E_0 suggests that mostly low energy particles are scattered and a high E_0 suggests that the scattering mechanism scatters low and high energy electrons. Reality is a bit more messy and a high E_0 may be a signature of a scattering mechanism preferential to high energy electrons, but is hidden by the convolution of the source particles available to be scattered (typically with a falling energy spectrum) and the energy-dependent scattering efficiency.

The short duration of microbursts observed by a single LEO satellite has an ambiguity when interpreting what is exactly a microburst. The two possible realities are: a microburst is very small and spatially stationary so that the LEO spacecraft

376 passes through it in less than a second. Alternatively, microbursts are spatially large
 377 with a short duration such that the microburst passes by the spacecraft in a fraction
 378 of a second. There are a few ways to distinguish between the two possible realities,
 379 and each one has a unique set of advantages.

380 A high altitude balloon provides essentially a stationary view of the precipitating
 381 particles under the radiation belt footprints so a short-lived, temporal microburst can
 382 be unambiguously identified. Spatial structures, on the other hand, are difficult to
 383 identify because a balloon is essentially still on drift timescales.

384 Multi-spacecraft missions are an alternate solution which can determine if a
 385 microburst-like feature is spatial or temporal. As will be shown in this dissertation,
 386 if a microburst is observed simultaneously by two spacecraft then it is temporal and
 387 has a size greater than the spacecraft separation. On the contrary, if two spacecraft
 388 observe a microburst-like feature at different times, but at the same location, then
 389 the feature is spatial and may be a curtain (Blake and O'Brien, 2016). Both balloon
 390 and multi-spacecraft observational methods have a unique set of strengths, and this
 391 dissertation takes the multi-spacecraft approach to identify and study microbursts.

392

Scope of Research

393 This dissertation furthers our understanding of the microburst scattering
 394 mechanism by observing the scattering directly, and measuring the microburst sizes
 395 and comparing them to the size of waves near the magnetic equator where those
 396 electrons could have been scattered. Chapter ?? describes a microburst scattering
 397 event observed by NASA's Van Allen Probes which was studied in the theoretic
 398 framework of pitch angle and energy diffusion. The following two chapters will then
 399 study the size of microbursts. Chapter ?? describes a bouncing packet microburst
 400 observation made by MSU's FIREBIRD-II mission where the microburst's lower

401 bound longitudinal and latitudinal sizes were estimated. Then Chapter ?? expands
402 the case study from Ch. ?? to a statistical study of microburst sizes using The
403 Aerospace Corporation's AeroCube-6 (AC6) CubeSats. In this study, a Monte Carlo
404 and analytic microburst size models were developed to account for the compounding
405 effects of random microburst sizes and locations. Lastly, Chapter ?? will summarize
406 the dissertation work and make concluding remarks regarding outstanding questions
407 in microburst physics.

Bibliography

- 409 Anderson, B., Shekhar, S., Millan, R., Crew, A., Spence, H., Klumpar, D., Blake, J.,
 410 O'Brien, T., and Turner, D. (2017). Spatial scale and duration of one microburst
 411 region on 13 August 2015. *Journal of Geophysical Research: Space Physics*.
- 412 Anderson, K. A. and Milton, D. W. (1964). Balloon observations of X rays in the
 413 auroral zone: 3. High time resolution studies. *Journal of Geophysical Research*,
 414 69(21):4457–4479.
- 415 Barcus, J., Brown, R., and Rosenberg, T. (1966). Spatial and temporal character of
 416 fast variations in auroral-zone x rays. *Journal of Geophysical Research*, 71(1):125–
 417 141.
- 418 Baumjohann, W. and Treumann, R. A. (1997). *Basic space plasma physics*. World
 419 Scientific.
- 420 Blake, J.,Looper, M., Baker, D., Nakamura, R., Klecker, B., and Hovestadt, D.
 421 (1996). New high temporal and spatial resolution measurements by sampex of the
 422 precipitation of relativistic electrons. *Advances in Space Research*, 18(8):171 – 186.
- 423 Blake, J. B. and O'Brien, T. P. (2016). Observations of small-scale latitudinal
 424 structure in energetic electron precipitation. *Journal of Geophysical Research: Space
 425 Physics*, 121(4):3031–3035. 2015JA021815.
- 426 Blum, L., Li, X., and Denton, M. (2015). Rapid MeV electron precipitation as
 427 observed by SAMPEX/HILT during high-speed stream-driven storms. *Journal of
 428 Geophysical Research: Space Physics*, 120(5):3783–3794. 2014JA020633.
- 429 Breneman, A., Crew, A., Sample, J., Klumpar, D., Johnson, A., Agapitov, O.,
 430 Shumko, M., Turner, D., Santolik, O., Wygant, J., et al. (2017). Observations
 431 directly linking relativistic electron microbursts to whistler mode chorus: Van allen
 432 probes and FIREBIRD II. *Geophysical Research Letters*.
- 433 Breneman, A. W., Halford, A., Millan, R., McCarthy, M., Fennell, J., Sample, J.,
 434 Woodger, L., Hospodarsky, G., Wygant, J. R., Cattell, C. A., et al. (2015). Global-
 435 scale coherence modulation of radiation-belt electron loss from plasmaspheric hiss.
 436 *Nature*, 523(7559):193.
- 437 Brown, R., Barcus, J., and Parsons, N. (1965). Balloon observations of auroral zone
 438 x rays in conjugate regions. 2. microbursts and pulsations. *Journal of Geophysical
 439 Research (U.S.)*.
- 440 Capannolo, L., Li, W., Ma, Q., Shen, X.-C., Zhang, X.-J., Redmon, R., Rodriguez,
 441 J., Engebretson, M., Kletzing, C., Kurth, W., et al. (2019). Energetic electron
 442 precipitation: multi-event analysis of its spatial extent during emic wave activity.
 443 *Journal of Geophysical Research: Space Physics*.

- 444 Claudepierre, S., O'Brien, T.,Looper, M., Blake, J., Fennell, J., Roeder, J.,
 445 Clemmons, J., Mazur, J., Turner, D., Reeves, G., et al. (2019). A revised look
 446 at relativistic electrons in the earth's inner radiation zone and slot region. *Journal*
 447 of *Geophysical Research: Space Physics*, 124(2):934–951.
- 448 Crew, A. B., Spence, H. E., Blake, J. B., Klumpar, D. M., Larsen, B. A., O'Brien,
 449 T. P., Driscoll, S., Handley, M., Legere, J., Longworth, S., Mashburn, K.,
 450 Mosleh, E., Ryhajlo, N., Smith, S., Springer, L., and Widholm, M. (2016). First
 451 multipoint in situ observations of electron microbursts: Initial results from the
 452 NSF FIREBIRD II mission. *Journal of Geophysical Research: Space Physics*,
 453 121(6):5272–5283. 2016JA022485.
- 454 Datta, S., Skoug, R., McCarthy, M., and Parks, G. (1997). Modeling of microburst
 455 electron precipitation using pitch angle diffusion theory. *Journal of Geophysical*
 456 *Research: Space Physics*, 102(A8):17325–17333.
- 457 Douma, E., Rodger, C., Blum, L., O'Brien, T., Clilverd, M., and Blake, J. (2019).
 458 Characteristics of relativistic microburst intensity from sampex observations.
 459 *Journal of Geophysical Research: Space Physics*.
- 460 Douma, E., Rodger, C. J., Blum, L. W., and Clilverd, M. A. (2017). Occurrence
 461 characteristics of relativistic electron microbursts from SAMPEX observations.
 462 *Journal of Geophysical Research: Space Physics*, 122(8):8096–8107. 2017JA024067.
- 463 Eastwood, J., Hietala, H., Toth, G., Phan, T., and Fujimoto, M. (2015). What
 464 controls the structure and dynamics of earths magnetosphere? *Space Science*
 465 *Reviews*, 188(1-4):251–286.
- 466 Greeley, A., Kanekal, S., Baker, D., Klecker, B., and Schiller, Q. (2019). Quantifying
 467 the contribution of microbursts to global electron loss in the radiation belts. *Journal*
 468 of *Geophysical Research: Space Physics*.
- 469 Hendry, A. T., Rodger, C. J., and Clilverd, M. A. (2017). Evidence of sub-mev
 470 emic-driven electron precipitation. *Geophysical Research Letters*, 44(3):1210–1218.
- 471 Horne, R., Glauert, S., Meredith, N., Boscher, D., Maget, V., Heynderickx, D., and
 472 Pitchford, D. (2013). Space weather impacts on satellites and forecasting the earth's
 473 electron radiation belts with spacecast. *Space Weather*, 11(4):169–186.
- 474 Horne, R. B., Thorne, R. M., Shprits, Y. Y., Meredith, N. P., Glauert, S. A., Smith,
 475 A. J., Kanekal, S. G., Baker, D. N., Engebretson, M. J., Posch, J. L., et al.
 476 (2005). Wave acceleration of electrons in the van allen radiation belts. *Nature*,
 477 437(7056):227.
- 478 Kasahara, S., Miyoshi, Y., Yokota, S., Mitani, T., Kasahara, Y., Matsuda, S.,
 479 Kumamoto, A., Matsuoka, A., Kazama, Y., Frey, H., et al. (2018). Pulsating
 480 aurora from electron scattering by chorus waves. *Nature*, 554(7692):337.

- 481 Klumpar, D., Springer, L., Mosleh, E., Mashburn, K., Berardinelli, S., Gunderson,
 482 A., Handly, M., Ryhajlo, N., Spence, H., Smith, S., Legere, J., Widholm, M.,
 483 Longworth, S., Crew, A., Larsen, B., Blake, J., and Walmsley, N. (2015). Flight
 484 system technologies enabling the twin-cubesat firebird-ii scientific mission.
- 485 Lee, J. J., Parks, G. K., Lee, E., Tsurutani, B. T., Hwang, J., Cho, K. S., Kim, K.-H.,
 486 Park, Y. D., Min, K. W., and McCarthy, M. P. (2012). Anisotropic pitch angle
 487 distribution of 100 keV microburst electrons in the loss cone: measurements from
 488 STSAT-1. *Annales Geophysicae*, 30(11):1567–1573.
- 489 Lee, J.-J., Parks, G. K., Min, K. W., Kim, H. J., Park, J., Hwang, J., McCarthy,
 490 M. P., Lee, E., Ryu, K. S., Lim, J. T., Sim, E. S., Lee, H. W., Kang, K. I., and
 491 Park, H. Y. (2005). Energy spectra of 170–360 keV electron microbursts measured
 492 by the korean STSAT-1. *Geophysical Research Letters*, 32(13). L13106.
- 493 Li, X., Selesnick, R., Schiller, Q., Zhang, K., Zhao, H., Baker, D. N., and Temerin,
 494 M. A. (2017). Measurement of electrons from albedo neutron decay and neutron
 495 density in near-earth space. *Nature*, 552(7685):382.
- 496 Lorentzen, K. R., Blake, J. B., Inan, U. S., and Bortnik, J. (2001a). Observations
 497 of relativistic electron microbursts in association with VLF chorus. *Journal of
 498 Geophysical Research: Space Physics*, 106(A4):6017–6027.
- 499 Lorentzen, K. R.,Looper, M. D., and Blake, J. B. (2001b). Relativistic electron
 500 microbursts during the GEM storms. *Geophysical Research Letters*, 28(13):2573–
 501 2576.
- 502 Lyons, L. R. and Thorne, R. M. (1973). Equilibrium structure of radiation belt
 503 electrons. *Journal of Geophysical Research*, 78(13):2142–2149.
- 504 Meredith, N., Horne, R., Summers, D., Thorne, R., Iles, R., Heynderickx, D., and
 505 Anderson, R. (2002). Evidence for acceleration of outer zone electrons to relativistic
 506 energies by whistler mode chorus. In *Annales Geophysicae*, volume 20, pages 967–
 507 979.
- 508 Millan, R. and Thorne, R. (2007). Review of radiation belt relativistic electron losses.
 509 *Journal of Atmospheric and Solar-Terrestrial Physics*, 69(3):362 – 377.
- 510 Nakamura, R., Baker, D. N., Blake, J. B., Kanekal, S., Klecker, B., and Hovestadt,
 511 D. (1995). Relativistic electron precipitation enhancements near the outer edge of
 512 the radiation belt. *Geophysical Research Letters*, 22(9):1129–1132.
- 513 Nakamura, R., Isowa, M., Kamide, Y., Baker, D., Blake, J., and Looper, M. (2000).
 514 Observations of relativistic electron microbursts in association with VLF chorus.
 515 *J. Geophys. Res.*, 105:15875–15885.

- 516 O'Brien, T., Claudepierre, S., Blake, J., Fennell, J. F., Clemons, J., Roeder, J.,
 517 Spence, H. E., Reeves, G., and Baker, D. (2014). An empirically observed pitch-
 518 angle diffusion eigenmode in the earth's electron belt near $l^* = 5.0$. *Geophysical*
 519 *Research Letters*, 41(2):251–258.
- 520 O'Brien, T., Claudepierre, S., Guild, T., Fennell, J., Turner, D., Blake, J., Clemons,
 521 J., and Roeder, J. (2016). Inner zone and slot electron radial diffusion revisited.
 522 *Geophysical Research Letters*, 43(14):7301–7310.
- 523 O'Brien, T. and Moldwin, M. (2003). Empirical plasmapause models from magnetic
 524 indices. *Geophysical Research Letters*, 30(4).
- 525 O'Brien, T. P.,Looper, M. D., and Blake, J. B. (2004). Quantification of relativistic
 526 electron microburst losses during the GEM storms. *Geophysical Research Letters*,
 527 31(4). L04802.
- 528 O'Brien, T. P., Lorentzen, K. R., Mann, I. R., Meredith, N. P., Blake, J. B., Fennell,
 529 J. F.,Looper, M. D., Milling, D. K., and Anderson, R. R. (2003). Energization of
 530 relativistic electrons in the presence of ULF power and MeV microbursts: Evidence
 531 for dual ULF and VLF acceleration. *Journal of Geophysical Research: Space*
 532 *Physics*, 108(A8).
- 533 Ozaki, M., Miyoshi, Y., Shiokawa, K., Hosokawa, K., Oyama, S.-i., Kataoka, R.,
 534 Ebihara, Y., Ogawa, Y., Kasahara, Y., Yagitani, S., et al. (2019). Visualization of
 535 rapid electron precipitation via chorus element wave–particle interactions. *Nature*
 536 *communications*, 10(1):257.
- 537 Parks, G. K. (1967). Spatial characteristics of auroral-zone X-ray microbursts. *Journal*
 538 *of Geophysical Research*, 72(1):215–226.
- 539 Reeves, G., Spence, H. E., Henderson, M., Morley, S., Friedel, R., Funsten, H., Baker,
 540 D., Kanekal, S., Blake, J., Fennell, J., et al. (2013). Electron acceleration in the
 541 heart of the van allen radiation belts. *Science*, 341(6149):991–994.
- 542 Reeves, G. D., McAdams, K. L., Friedel, R. H. W., and O'Brien, T. P. (2003). Ac-
 543 celeration and loss of relativistic electrons during geomagnetic storms. *Geophysical*
 544 *Research Letters*, 30(10):n/a–n/a. 1529.
- 545 Schulz, M. and Lanzerotti, L. J. (1974). *Particle Diffusion in the Radiation Belts*.
 546 Springer.
- 547 Seppälä, A., Douma, E., Rodger, C., Verronen, P., Clilverd, M. A., and Bortnik, J.
 548 (2018). Relativistic electron microburst events: Modeling the atmospheric impact.
 549 *Geophysical Research Letters*, 45(2):1141–1147.

- 550 Spence, H. E., Blake, J. B., Crew, A. B., Driscoll, S., Klumpar, D. M., Larsen,
 551 B. A., Legere, J., Longworth, S., Mosleh, E., O'Brien, T. P., Smith, S., Springer,
 552 L., and Widholm, M. (2012). Focusing on size and energy dependence of electron
 553 microbursts from the van allen radiation belts. *Space Weather*, 10(11).
- 554 Summers, D. (2005). Quasi-linear diffusion coefficients for field-aligned electro-
 555 magnetic waves with applications to the magnetosphere. *Journal of Geophysical
 556 Research: Space Physics*, 110(A8):n/a–n/a. A08213.
- 557 Summers, D., Thorne, R. M., and Xiao, F. (1998). Relativistic theory of wave-particle
 558 resonant diffusion with application to electron acceleration in the magnetosphere.
 559 *Journal of Geophysical Research: Space Physics*, 103(A9):20487–20500.
- 560 Thorne, R. M., O'Brien, T. P., Shprits, Y. Y., Summers, D., and Horne, R. B. (2005).
 561 Timescale for MeV electron microburst loss during geomagnetic storms. *Journal
 562 of Geophysical Research: Space Physics*, 110(A9). A09202.
- 563 Trefall, H., Bjordal, J., Ullaland, S., and Stadsnes, J. (1966). On the extension of
 564 auroral-zone x-ray microbursts. *Journal of Atmospheric and Terrestrial Physics*,
 565 28(2):225–233.
- 566 Tsurutani, B. T. and Lakhina, G. S. (1997). Some basic concepts of wave-particle
 567 interactions in collisionless plasmas. *Reviews of Geophysics*, 35(4):491–501.
- 568 Ukhorskiy, A. Y., Anderson, B. J., Brandt, P. C., and Tsyganenko, N. A. (2006).
 569 Storm time evolution of the outer radiation belt: Transport and losses. *Journal of
 570 Geophysical Research: Space Physics*, 111(A11):n/a–n/a. A11S03.
- 571 Van Allen, J. A. (1959). The geomagnetically trapped corpuscular radiation. *Journal
 572 of Geophysical Research*, 64(11):1683–1689.
- 573 Vernov, S. and Chudakov, A. (1960). Investigation of radiation in outer space. In
 574 *International Cosmic Ray Conference*, volume 3, page 19.
- 575 Walker, A. D. M. (1993). *Plasma waves in the magnetosphere*, volume 24. Springer
 576 Science & Business Media.